THE JOURNAL OF BIOLOGICAL CHEMISTRY VOL. 290, NO. 6, pp. 3183–3196, February 6, 2015

Crystal Structure of Subunits D and F in Complex Gives Insight into Energy Transmission of the Eukaryotic V-ATPase from *Saccharomyces cerevisiae*[*◆]

Received for publication, October 30, 2014, and in revised form, November 26, 2014 Published, JBC Papers in Press, December 12, 2014, DOI 10.1074/jbc.M114.622688

Asha Manikkoth Balakrishna[1], **Sandip Basak**[1,2], **Malathy Sony Subramanian Manimekalai, and Gerhard Grüber**[3]

From the School of Biological Sciences, Nanyang Technological University, 60 Nanyang Drive, Singapore 637551, Republic of Singapore

Background: Subunits D and F are essential in ATP hydrolysis and reversible disassembly of V_1V_O-ATPases.
Results: First crystallographic structure of eukaryotic V-ATPase subunit D and entire subunit F is presented.
Conclusion: Structural elements in subunits D and F enable the DF assembly to become a central motor element in the engine V-ATPase.
Significance: Mechanistic understanding of the subunit DF assembly and its key roles in enzyme catalysis and regulation are presented.

Eukaryotic V_1V_O-ATPases hydrolyze ATP in the V_1 domain coupled to ion pumping in V_O. A unique mode of regulation of V-ATPases is the reversible disassembly of V_1 and V_O, which reduces ATPase activity and causes silencing of ion conduction. The subunits D and F are proposed to be key in these enzymatic processes. Here, we describe the structures of two conformations of the subunit DF assembly of *Saccharomyces cerevisiae* (*Sc*DF) V-ATPase at 3.1 Å resolution. Subunit D (*Sc*D) consists of a long pair of α-helices connected by a short helix (^{79}IGYQVQE^{85}) as well as a β-hairpin region, which is flanked by two flexible loops. The long pair of helices is composed of the N-terminal α-helix and the C-terminal helix, showing structural alterations in the two *Sc*DF structures. The entire subunit F (*Sc*F) consists of an N-terminal domain of four β-strands (β1–β4) connected by four α-helices (α1–α4). α1 and β2 are connected via the loop ^{26}GQITPETQEK^{35}, which is unique in eukaryotic V-ATPases. Adjacent to the N-terminal domain is a flexible loop, followed by a C-terminal α-helix (α5). A perpendicular and extended conformation of helix α5 was observed in the two crystal structures and in solution x-ray scattering experiments, respectively. Fitted into the nucleotide-bound A_3B_3 structure of the related A-ATP synthase from *Enterococcus hirae*, the arrangements of the *Sc*DF molecules reflect their central function in ATPase-coupled ion conduction. Furthermore, the flexibility of the terminal helices of both subunits as well as the loop ^{26}GQITPETQEK^{35} provides information about the regulatory step of reversible V_1V_O disassembly.

Eukaryotic V-ATPases (V_1V_O-ATPases)[4] are ATP-driven ion pumps, which generate an electrochemical proton gradient or proton-motive force across the membranes, leading to acidification of intracellular compartments (1, 2). Intracellular compartments of eukaryotic cells require the maintenance of acidic luminal pH by V-ATPase. The enzyme is also targeted to the plasma membrane and is involved in extracellular acidification of some specialized cells in the kidney, epididymis, and bone tissues (3). The V-ATPase acidifies the extra-tumoral environment in cancer (4). The pH becomes more acidic as the exocytic and endocytic vesicular trafficking pathways reach their destination (5). The regulation of V-ATPase function and V-ATPase-driven differential acidification is described to be achieved by the following: (*a*) modulation of V-ATPase dependent acidification via a chemiosmotic mechanism; (*b*) regulation of coupling of the V-ATPase; (*c*) subunit-specific targeting of V-ATPase; and (*d*) regulation of V-ATPase activity via reversible dissociation of the V_1 and V_O parts of the protein (5).

Eukaryotic V-ATPases consist of 14 different subunits $A_3B_3CDE_3FG_3Hac_xc_y'c_z''d, e$, where the stoichiometry (*x,y,z*) of the *c*, *c*′, and *c*′ subunits are not known (6). Many of these subunits are present in multiple isoforms (3, 7). V_1V_O-ATPases have a bipartite structure consisting of a soluble cytoplasmic V_1 domain (subunits $A_3B_3CDE_3FG_3H$) and a membrane-integrated V_O domain (subunits *a*, *c*, *c*′, *c*″, *d*, *e*). Electron microscopy image analysis (8–11) and small-angle x-ray scattering (SAXS) (12, 13) have provided a general outline for the structural organization of the V_1 and V_O parts as well as the entire enzyme (Fig. 1). Both parts are linked by connecting regions that are important for coupling ion translocation in V_O with ATP hydrolysis in V_1 and are proposed to be involved in regulating the activity of the enzyme by reversible disassembly. These connecting regions consist of the central stalk subunits (D, F, and *d*) and peripheral stalk subunits (E, G, C, H, *e*, and *a*).

* This work was supported in part by the Ministry of Education, Singapore, Grants MOE2011-T2-2-156 and ARC 18/12 (to G. G.).
◆ This article was selected as a Paper of the Week.
The atomic coordinates and structure factors (code 4RND) have been deposited in the Protein Data Bank (http://wwpdb.org/).
[1] Both authors contributed equally to this work.
[2] Recipient of a research scholarship from the Nanyang Technological University.
[3] To whom correspondence should be addressed. Tel.: 65-6316-2989; Fax: 65-6791-3856; E-mail: ggrueber@ntu.edu.sg.

[4] The abbreviations used are: V-ATPase, V_1V_O-ATPase; SAXS, small angle x-ray scattering; r.m.s.d., root mean square deviation; MAD, multiwavelength anomalous dispersion; AMP-PNP, adenosine 5′-(β,γ-imino)triphosphate.

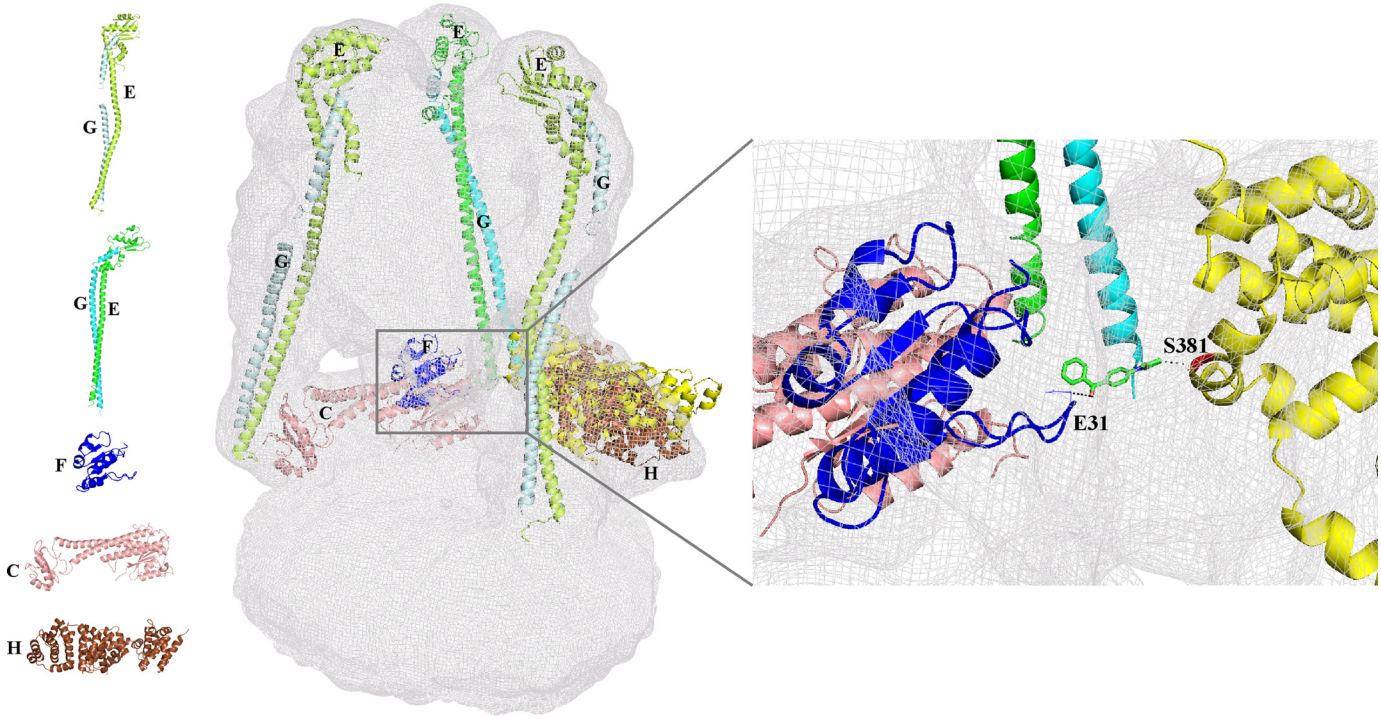

FIGURE 1. **Arrangement of the existing individual atomic subunit structures in the EM map of the *S. cerevisiae* V-ATPase.** Subunits C (1U7L; *salmon*), H (1HO8, *brown*), and F(1–94) (4IX9, *blue*) from *S. cerevisiae* were fitted into the EM map. The two conformations of EG subunits, the straight (4DL0; *green* and *cyan*) and more bent (4EFA; *lemon* and *pale cyan*) are fitted to the three peripheral stalks. *Inset,* region of the EM map showing the interaction of modeled subunit H (Ser-381) (*yellow*) through the sulfhydryl cross-linker 4-(*N*-maleimido)benzophenone (62) (*stick*; *green*) to the *S. cerevisiae* subunit F(1–94) (Glu-31). *Left panel,* schematic representation of the structures of the individual *S. cerevisiae* subunits C (1U7L; *salmon*), F(1–94) (4IX9, *blue*), H (1HO8, *brown*), and EG in two conformations, straight (4DL0; *green* and *cyan*) and bent (4EFA; *lemon* and *pale cyan*).

In the last decade, the structures of the individual eukaryotic V-ATPase subunits C (14), E (15–17), F(1–94) (18), G (15, 19, 20), and H (21) were determined, all from the *Saccharomyces cerevisiae* enzyme. These structures fit into a cryo-EM map of the *S. cerevisiae* V-ATPase as shown in Fig. 1.

During catalysis the central stalk subunit F is proposed to undergo structural alterations by interacting with subunits A, B, D, and *d* in a nucleotide-dependent manner (22, 23). Most recently, we determined the crystallographic structure of the N-terminal 94 amino acids domain (*Sc*F(1–94)) of the 118-residue *S. cerevisiae* subunit F (18). *Sc*F(1–94) has an elliptical shape with a size of 30 × 16 × 38 Å (Fig. 1). It contains four-parallel β-strands, which are intermittently surrounded by four α-helices forming an egg-shaped structure. Unknown so far are the structures of the C-terminal domain of *Sc*F as well as the structure of the entire subunit D. Both are described as the key elements in coupling ATPase activity in the A_3B_3 headpiece via a rotary-like mechanism with ion conduction in the V_O part (24). Furthermore, subunit F has been proposed to transmit the signal for V_1V_O disassembly by interacting with stalk subunit H and the nucleotide-binding subunits A and B in the V_1 part (4, 11, 18).

Understanding the enzymatic and regulatory functions of the two stalk subunits D and F requires knowledge of their high resolution structure. Here, we present the first structural models of the *S. cerevisiae* DF assembly (*Sc*DF) at a resolution of 3.1 Å. The structural models of *Sc*DF show the molecular interactions between both subunits as well as the catalytic A_3B_3 headpiece of the V-ATPase, and they provide important insight into an interface essential for the structural integrity of the enzyme. Finally, the new structures shed light onto the coupling events of ATP-dependent ion pumping and reversible disassembly.

EXPERIMENTAL PROCEDURES

Biochemicals—Chemicals of analytical grade were obtained from Biomol (Hamburg, Germany), Merck, Sigma, or Serva (Heidelberg, Germany). Nickel-nitrilotriacetic acid chromatography resin and chemicals for SDS-PAGE were obtained from Qiagen (Hilden, Germany) and Bio-Rad, respectively.

Purification of the S. cerevisiae V-ATPase DF Assembly—Cloning, production, and purification of the recombinant DF heterodimer of the *S. cerevisiae* V-ATPase (*Sc*DF) has been described previously (18). The selenomethionine DF assembly was produced in *E. coli* strain BL21 (DE3) cells by growing 5-ml culture cells overnight at 37 °C in Luria-Bertani (LB) medium, which contained 100 μg/ml carbenicillin. The cells were pelleted by centrifugation (6,000 × *g*), resuspended in M9 minimal media, pelleted (1,000 × *g*), and resuspended twice. The cell suspension was used to inoculate 1 liter of pre-warmed (37 °C) M9 minimal media and grown at 37 °C. When the A_{600} of 0.6 was obtained, the minimal media were supplemented with 100 mg/liter lysine, phenylalanine, and threonine, 50 mg of isoleucine, leucine, and valine, and 25 mg of selenomethionine and incubated for 15 min. Thereafter, protein production was induced by the addition of isopropyl β-D-thiogalactopyranoside to a final concentration of 0.8 mM, and growth was continued at 37 °C for 4 h. The selenomethionine-substituted *Sc*DF was purified as described earlier (18), except that 1 mM dithio-

threitol (DTT) was used in all buffers to avoid oxidation of selenium.

Crystallization of the DF Heterodimer—Crystallization of the native *Sc*DF was done using the vapor diffusion method and commercially available screens. Hanging drops were set up by mixing 1 μl of the purified *Sc*DF (5 mg/ml and 8 mg/ml) in buffer, 50 mM Tris/HCl, pH 8.5, 250 mM NaCl, 5 mM EDTA with 1 μl of the precipitant solution and incubated at 18 °C against 500 μl of mother liquor. Initial crystals were obtained in Hampton research crystal screen 1, condition 11 (0.1 M sodium citrate tribasic dehydrate, pH 5.6, 1.0 M ammonium phosphate monobasic). Good diffraction quality crystals were obtained in optimized condition of 0.1 M sodium citrate tribasic dehydrate, pH 5.6, 1.2 M ammonium citrate monobasic. The crystals were flash-frozen in liquid nitrogen at 100 K in crystallization buffer containing 25% (v/v) glycerol. For the selenomethionine *Sc*DF, the final buffer was exchanged with 50 mM Tris/HCl, pH 8.5, 250 mM NaCl, 5 mM EDTA, and 2 mM tris(2-carboxyethyl)-phosphine (TCEP). Further optimization was done using additives from Hampton research, and the crystals, grown in the presence of 3-(1-Pyridino)-1-propane sulfonate (NDSB), were finally used for structural studies.

Data Collection and Processing of X-ray Diffraction Data—X-ray diffraction data for the native *Sc*DF crystal was collected at the National Synchrotron Radiation Research Centre, Taiwan. Initial attempts to get a solution by molecular replacement, using the subunit DF structures of related *Enterococcus hirae* A-ATP-synthase (3AON and 3VR4 (25, 26)) and *Thermus thermophilus* (3W3A (27)), as well as the *S. cerevisiae* mutant structure, $ScF_{I\text{-}94}$ (4IX9) (18), were unsuccessful. Therefore, selenomethionine crystals of *Sc*DF were produced as described above, and multiwavelength anomalous dispersion (MAD) data were collected at the synchrotron beamline 13B1 of the National Synchrotron Radiation Research Centre in Taiwan using the Q315 detector. Three datasets were collected to a 3.1 Å resolution from a single crystal at the appropriate inflection, peak, and remote wavelengths that were selected from a selenium absorption spectrum. Data were collected as a series of 0.5 oscillation images covering a crystal rotation range of 200 on cryo-cooled crystals at 100 K. The MAD dataset was indexed, integrated, and scaled using the HKL2000 suite of programs (28). The data were cut off at 3.1 Å based on the $CC_{1/2}$ statistics (29) (correlation coefficient between two random halves of the data set where $CC_{1/2} > 10\%$) to determine the high resolution cutoff for our data. Phenix (30) was used to compute the $CC_{1/2}$ (78.7% for the highest resolution shell and 99.9% for the entire data set), supporting our high resolution cutoff determination.

The structure of *Sc*DF was phased by the single wavelength anomalous diffraction method, using the peak dataset at 3.1 Å of the selenomethionine MAD data set. The Shelx program (31) and the Autorickshaw server were used to identify 5 out of 14 selenium sites in the protein (32, 33). The resulting phases were channeled into Pirate for density modification (34), and automated model building was done using Buccaneer of CCP4 suite (35). Manual correction of the model was done with COOT (36), and refinement was carried out using REFMAC of the CCP4 suite (37). A final check on the stereochemical quality of the final model was assessed using PROCHECK (38) and Molprobity (39), and any conflicts were addressed. Molprobity analysis indicated that the overall geometry of the final model was ranked in the 100th percentile (Molprobity score of 1.69). The clash score for all atoms was 2.87 corresponding to a 100th percentile ranking of structures of comparable resolution. All the figures were drawn using the program PyMOL (40). The structure refinement statistics are given in Table 1. The atomic coordinates and structure factors have been deposited in the Protein Data Bank with accession code 4RND.

Solution Small Angle X-ray Scattering of Subunit F—SAXS data of recombinant subunit F of the *S. cerevisiae* V-ATPase (*Sc*F), purified according to Basak *et al.* (18), were measured with the Bruker NANOSTAR SAXS instrument, equipped with a MetalJet x-ray source and Vantec 2000 detector system (41). The x-ray radiation was generated from a liquid gallium alloy with microfocus x-ray source (K_α = 1.3414 Å with a potential of 70 kV and a current of 2.857 mA). The x-rays are filtered through Montel mirrors and collimated by the two-pinhole system. The sample to detector distance was set at 67 cm, and the sample chamber and x-ray paths were evacuated. Protein concentrations of 2.0 and 4.2 mg/ml of *Sc*F have been measured at 15 °C with a sample volume of 40 μl in a vacuum tight quartz capillary. The buffer containing 50 mM Tris, pH 7.5, 200 mM NaCl, and 5 mM EDTA was measured twice. For each measurement, a total of six measurements at 5-min intervals were recorded. The data were flood-field, spatially corrected, and processed using the inbuilt SAXS software. The data were tested for possible radiation damage by comparing the six data sets, and no changes were detected. The scattering of the buffer was subtracted, and the difference curves were scaled for the concentration. All the data processing steps were performed automatically using the program package PRIMUS (42). The experimental data obtained for different concentrations were analyzed for aggregation and folding state using Guinier (43) and Kartky plots (44), respectively. The forward scattering $I(0)$ and the radius of gyration R_g were evaluated using the Guinier approximation (43). These parameters were also computed from the entire scattering patterns using the indirect transform package GNOM (45), which also provided the distance distribution function $p(r)$, which gives the maximal particle diameter, D_{max}. The hydrated volume Vp, used to estimate the molecular mass of globular proteins, was computed using the Porod invariant. Empirically, it was found that the hydrated volume in cubic nanometers should numerically be between 1.5 and 2 times the molecular mass in kilodaltons (46). Low resolution models of subunit F were built by the program DAMMIN (47). *Ab initio* solution shapes of subunit F were obtained by superposition of 10 independent model reconstructions with the program package SUBCOMP (48) and building an averaged model from the most probable one using the DAMAVER program (49).

Comparison of the experimental scattering curve with the theoretical scattering curves calculated for the monomer of subunit F with both conformations, parallel and perpendicular, were performed with CRYSOL (50). The dimer of subunit F in parallel or perpendicular conformation and a dimer model containing both conformations in one were modeled based on the truncated crystal structure of *S. cerevisiae* F(1–94) (Protein

TABLE 1
Statistics of data collection, processing, and refinement for SeMet *Sc*DF

	Peak	Inflection	Remote
Wavelength (Å)	0.978	0.979	0.963
Space group	$P6_1$	$P6_1$	$P6_1$
Unit cell parameters (Å)			
$a = b$ (Å)	168.063	168.34	168.47
c (Å)	128.629	128.68	128.86
$\alpha = \beta$ (°)	90	90	90
γ (°)	120	120	120
Solvent content (%)	80.27	80.31	80.38
No. of molecules in the asymmetric unit	2	2	2
Resolution range (Å)	30–3.1 (3.25–3.17)[a]	30–3.5 (3.73–3.6)[a]	30–3.6 (3.73–3.6)[a]
Total no. of reflections	425,295	79,622	72,990
No. of unique reflections	38,345	27,857	21,998
I/σ^a	19.1 (1.2)	10.1 (0.5)	9.6 (1.2)
Completeness (%)	99.0 (90.1)	94.6 (73.6)	97.9 (93.6)
R_{merge}[b] (%)	9.9 (84.9)	12.1 (73.7)	17.0 (82.7)
Multiplicity	11.4 (8.7)	4.8 (4.0)	4.7 (3.8)
$CC_{1/2}$	99.9 (78.7)	99.9 (69.3)	99.9 (63.7)
Refinement statistics			
R-factor[c] (%)	20.4		
R-free[d] (%)	23.2		
No. of waters	59		
No. of glycerols	3		
MolProbity statistics			
Ramachandran favored (%)	97.37		
Ramachandran outliers (%)	0		
Clash score	2.87		
r.m.s.d.			
Bond lengths (Å)	0.006		
Bond angles (°)	1.043		
Overall *B* values			
From Wilson plot (Å^2)	56		
Mean B value (Å^2)	37		

[a] Values in parentheses refer to the corresponding values of the highest resolution shell.
[b] $R_{merge} = \Sigma\Sigma_i|I_h - I_{hi}|/\Sigma\Sigma_i I_h$, where I_h is the mean intensity for reflection h.
[c] R-factor $= \Sigma||F_o| - |F_c||/\Sigma|F_o|$, where F_o and F_c are measured and calculated structure factors, respectively.
[d] R-free $= \Sigma||F_o| - |F_c|/\Sigma|F_o|$, calculated from 5% of the reflections selected randomly and omitted during refinement.

Data Bank code 4IX9 (18)), and their theoretical scattering curves were computed. Analysis showed that the dimer (parallel $\chi = 1.85$; perpendicular $\chi = 2.05$; both $\chi = 1.93$) had a better fit than the monomer (parallel $\chi = 2.20$; perpendicular $\chi = 2.08$). The models were then used in OLIGOMER (42) to find the best fit to a multicomponent mixture of proteins. A fit of $\chi = 1.62$ was achieved when both conformations of the dimer were present in equal amounts (perpendicular to parallel conformation of 51:49%), and no monomers were present. A dimer model was generated using CORAL (52) allowing flexibility for the loop (95–105) between the globular domain and the C-terminal helix (52).

RESULTS

Crystallographic Data of the ScDF Heterodimer—The complex of the subunits D (256 residues) and F (118 residues) of the *S. cerevisiae* V-ATPase was crystallized in the hexagonal space group $P6_1$, and its structure was determined by selenium SAD method and refined to 3.1 Å resolution. Assuming two *Sc*DF molecules in the asymmetric unit, the solvent content was 80.27% and the V_m was 6.09 Å^3 (53). The two molecules of *Sc*DF (called *Sc*DF1 and *Sc*DF2) are arranged in a head to tail orientation in the asymmetric unit (Fig. 2*A*). The final asymmetric unit consists of two molecules of *Sc*DF and 59 molecules of water and 3 glycerol molecules (Fig. 2*A*). The final R-factor and R-free (calculated with 5% of reflections that were not included in the refinement) were 0.20 and 0.22, respectively. In the *Sc*DF1 and *Sc*DF2 molecules, the residues 27–204 and 37–203 of the 256 amino acid subunit D were assigned, respectively. In the case of *Sc*DF1, all 118 residues of subunit F were resolved in the structure, whereby amino acids 1–116 could clearly be assigned in the *Sc*DF2 molecule. The side chain densities for all the amino acids are well resolved. Ramachandran restraints were turned on during real space refinement in Coot (36). Validation with the ERRAT server (54) gave an overall quality factor of 94%.

Overall Structure of ScDF—The overall structure of *S. cerevisiae* DF assembly is shown in Fig. 2*B*. Subunit D of the *S. cerevisiae* V-ATPase consists of a long pair of α-helices (110 Å), connected by a short helix (^{79}IGYQVQE^{85}) as well as a β-hairpin region, which is flanked by two flexible loops. The long pair of helices is composed of the N-terminal α-helix, which commences from Tyr-29 to Thr-75, and the C-terminal helix, containing residues Gly-128 to Arg-202. The remaining portion containing residues 76–127 is composed of a short β-hairpin region formed by residues Phe-92 to Ile-113, two flexible loops, and a short α-helix. The N-terminal helix consists of both hydrophobic residues and hydrophilic residues and is slightly basic. The short helix (^{79}IGYQVQE^{85}) is slightly acidic (Fig. 2*B*). The β-hairpin region contains hydrophobic and hydrophilic residues. The C-terminal helix mostly contains acidic residues. There is a slight bend in the C-terminal helix near the hinge region where a conserved Pro-179 is located. In comparison, a clear break can be seen in the same position of this helix near the proline-induced hinge region of the *Sc*DF2 molecule.

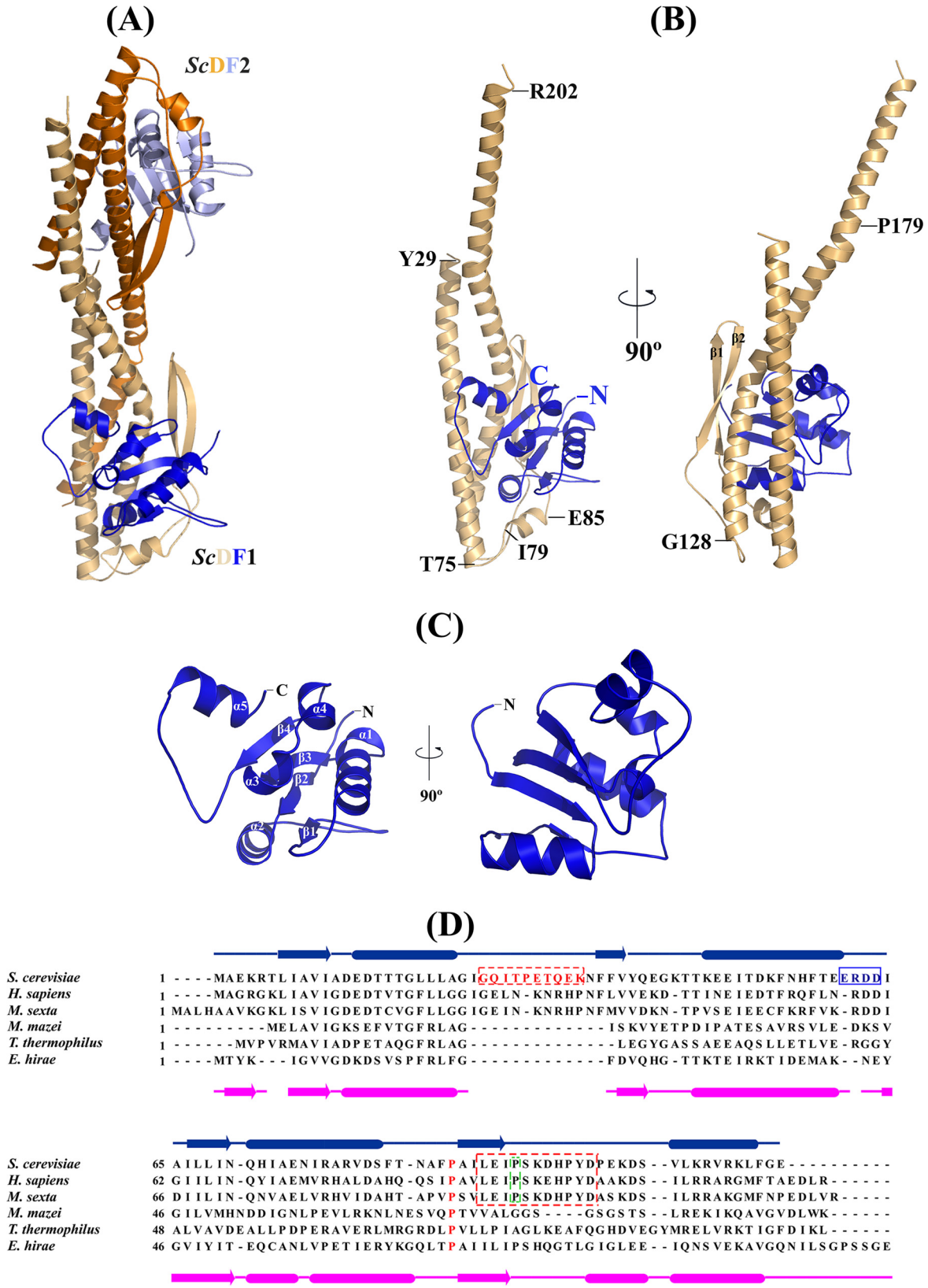

FIGURE 2. **Crystal structure of *S. cerevisiae* subunit DF complex.** *A,* crystal structure of DF complex of the *S. cerevisiae* V-ATPase in an asymmetric unit; *Sc*DF1 is shown in *wheat* and *blue*, and *Sc*DF2 is shown in *orange* and *light blue*, respectively. *B,* schematic representation of the *Sc*DF1 complex; *Sc*D and *Sc*F are shown in *wheat* and *dark blue*, respectively. Proline 179, which is conserved in all the eukaryotic ATP synthases, is labeled. *C,* schematic representation of *Sc*F1 (*dark blue*), with the unique C terminus helix conformation and the α-helices and β-strands labeled. *D,* sequence alignment of subunit F from different ATPases. The secondary structure elements of subunit F from *E. hirae* and *S. cerevisiae* are shown. The conserved sequence in the eukaryotic ATP synthase is shown within the *box*. The ^{26}GQITPETQEK^{35} loop of the F subunit is highlighted in *red*. The conserved Pro-89 is highlighted in *red* and is present in V-ATPases as well as A-ATP synthases. Proline 95, which is conserved in eukaryotic V ATPases, is highlighted by a *green frame*.

The r.m.s.d. value between the D subunit of the *Sc*DF1 and *Sc*DF2 molecule for 161 Cα atoms is 6.3 Å, compared with an r.m.s.d. of 1.0 Å for the first 117 equivalent Cα atoms of subunit D. These data indicate that movement of the C-terminal helix occurs around the hinge region of subunit D with maximum movement beginning after residue Ala-155.

The 118-residue-long subunit F of the *S. cerevisiae* V-ATPase reveals four parallel β-strands, which are enveloped by five α-helices (Fig. 2*C*). The four β-strands (β1–β4) are arranged parallel to each other and are connected by five α-helices (α1–α5). In both molecules, the conformation is similar except for the α5-helix. The four β-strands (β1, Leu-7 to Ala-12; β2, Phe-37 to Val-39; β3, Ile-64 to Asn-70, and β4, Ala-90 to Ile-94) and the four α-helices (α1, Glu-14 to Ala-23; α2, Lys-47 to Glu-60; α3, Gln-71 to Glu-75, and α4, Arg-78 to Ser-83) form the N-terminal globular domain. This N-terminal domain is connected via a flexible loop of 12 residues (Pro-95 to Asp-106) to the C-terminal α-helix (α5, residues Ser-107 to Leu-115). As confirmed by amino acid sequence alignment, the subunit F structure contains a unique loop between α1 and β2 (^{26}GQITPETQEK^{35}) and a highly conserved loop with a ^{60}ERDD^{63} motif between α2 and β3, which are present only in eukaryotic V-ATPases (Fig. 2*D*). The C-terminal helix α5 consists of mostly positively charged residues (^{107}SVLKRVRKL^{115}). The r.m.s.d. (Cα) between the 115 residues of subunit F of the *Sc*DF1 and *Sc*DF2 molecule is 3.5 Å. In comparison, the r.m.s.d. of the N-terminal 94 Cα atoms of subunit F in both molecules (*Sc*DF1 and *Sc*DF2) is 0.3 Å, reflecting that the maximum differences are prevailing in the C-terminal region. As shown in Fig. 4*A*, the flexible loop (Pro-95 to Asp-106) of subunit F in the *Sc*DF1 molecule is bent at residue Lys-105, causing a perpendicular orientation of its C-terminal helix α5 relative to the N- and C-terminal helices of subunit D. In comparison, in the *Sc*DF2 molecule the C-terminal helix α5 of subunit F is almost parallel to the N- and C-terminal helices of subunit D.

The overall surface electrostatic potential of *Sc*DF is composed of both acidic and basic residues except the exposed N- and C-terminal helix of subunit D, which are basic and predominantly acidic, respectively (Fig. 3, *A* and *B*). The electrostatic potential of the bottom of *Sc*DF is also composed of both acidic and basic residues. The hydrophobic residues are mostly found in the interface region of subunits D and F (Fig. 3*A*). In *Sc*D the hydrophobic site includes residues Leu-31, Leu-32, Lys-33, Leu-39, Phe-43, Thr-47, Ile-50, Met-57, Met-61, Ala-64, Leu-68, Val-71, and Ala-74 of the N-terminal α1-helix; amino acids Phe-92, Val-94, Ala-96, Val-101, Val-104, Leu-106, and Phe-109 of the β-hairpin region; and residues Val-143, Thr-145, Leu-146, Leu-149, Leu-152, Phe-156, Ile-157, and Leu-159 of the C-terminal helix α3. In the case of subunit F, the hydrophobic site is formed by the residues Ile-8, Ala-9, Val-10, Ile-11 and Ala-12 located of β1; Ile-64, Ala-65, Ile-66, Leu-67 and Leu-68 on β3; Ala-90, Ile-91, Leu-92, and Ile-94 of β4; and the residues Gly-19, Leu-20, Leu-21, and Leu-22 of the N-terminal helix α1.

Interaction of Subunits D and F—As revealed by Fig. 4*A*, the *S. cerevisiae* subunit F is bound to the lower middle part of subunit D. The hydrophobic residues from the C-terminal helix α3 of subunit D and α1 as well as β4 of subunit F, respectively, generate the major contacts of the hydrophobic interface of both subunits. A second point of interaction is formed by the ^{26}GQITPETQEK^{35} loop, which is in close proximity with the loop residues ^{85}ESVSTARFK^{94} of subunit D, which span the short helix (^{79}IGYQVQE^{85}) and the β-hairpin (Fig. 4*B*). In addition, the C-terminal helix α5 of subunit F of the *Sc*DF1 and *Sc*DF2 molecule is interacting with the N- and C-terminal helix of subunit D. In the case of the *Sc*DF1 molecule, the interaction of subunit D and F occurs via the amino acids Asp-51, Asp-160, and Lys-54 and Arg-111, Arg-113, and Asp-102 of subunits D and F, respectively (Fig. 4*B*). In comparison, residues Asp-160 and Thr-47 interact with Arg-111 and Arg-113 of subunits D and F for the *Sc*DF2 molecule (Fig. 4*C*). The existence of these two conformations of helix α5 of subunit F relative to the termini of subunit D indicates a very flexible conformational switching between an extended and slight compact conformation of subunit F.

Subunit F in Solution Studied by SAXS—The two conformations of the C terminus of the *Sc*F structures may also represent intermediate conformations that arise during movement about the hinge regions. To understand whether subunit F is able to undergo structural alterations in solution, SAXS experiments were performed. SAXS patterns of recombinant subunit F of the *S. cerevisiae* V-ATPase (*Sc*F) were recorded at 2.0 and 4.2 mg/ml, which showed similar final composite scattering curves (Fig. 5*A* and Table 2). The Guinier plots at low angles are linear and revealed good data quality with no indication of protein aggregation (Fig. 5*A*, *inset*). The Kratky plot ($I(s) \times s^2$ *versus* s) (Fig. 5*B*, *inset*) shows a bell-shaped peak at low angles indicating a well folded protein. The radius of gyration (R_g) values from the Guinier approximation were consistent at the two concentrations measured with a value of 19.3 ± 0.6 Å. The distance distribution functions ($p(r)$) were similarly shaped for the concentrations used (Fig. 5*B*), and the maximum particle dimension is D_{max} = 67.5 ± 3 Å. The gross shape of the subunit F was *ab initio* reconstructed and had a good fit to the experimental data in the entire scattering range and had a discrepancies of χ^2 = 0.951. Ten independent reconstructions produced similar envelope with normalized spatial discrepancy of 0.65 ± 0.01, and the average structure is shown in Fig. 5*D*.

The molecular mass as determined by the I_0 value, Porod hydrated volume, and from the SAXS MoW server (55) ranged from 21 to 24 kDa, indicating the presence of a dimer or a mixture of both monomer and dimer in solution. Comparison of the theoretical scattering curves for the monomer and dimer in both parallel and perpendicular conformations in CRYSOL confirmed the presence of dimer formation with the fit being improved when both conformations of the dimer were present in equal amounts. Based on the above observation, a dimer model was generated using CORAL (52), which allows flexibility for the loop with the residues 95–105 between the globular domain and the C-terminal helix α5 of *Sc*F. This program performs modeling of complexes against the experimental SAXS data using a combined rigid body for the atomic structures of the domains and the *ab initio* modeling of the unknown loop regions. The CORAL model fits with χ = 1.24 and reveals that the two conformations (parallel and perpendicular) co-exists in the same dimer with the C terminus being more compact in one and more extended in another molecule of the dimer (Fig. 5, *C*

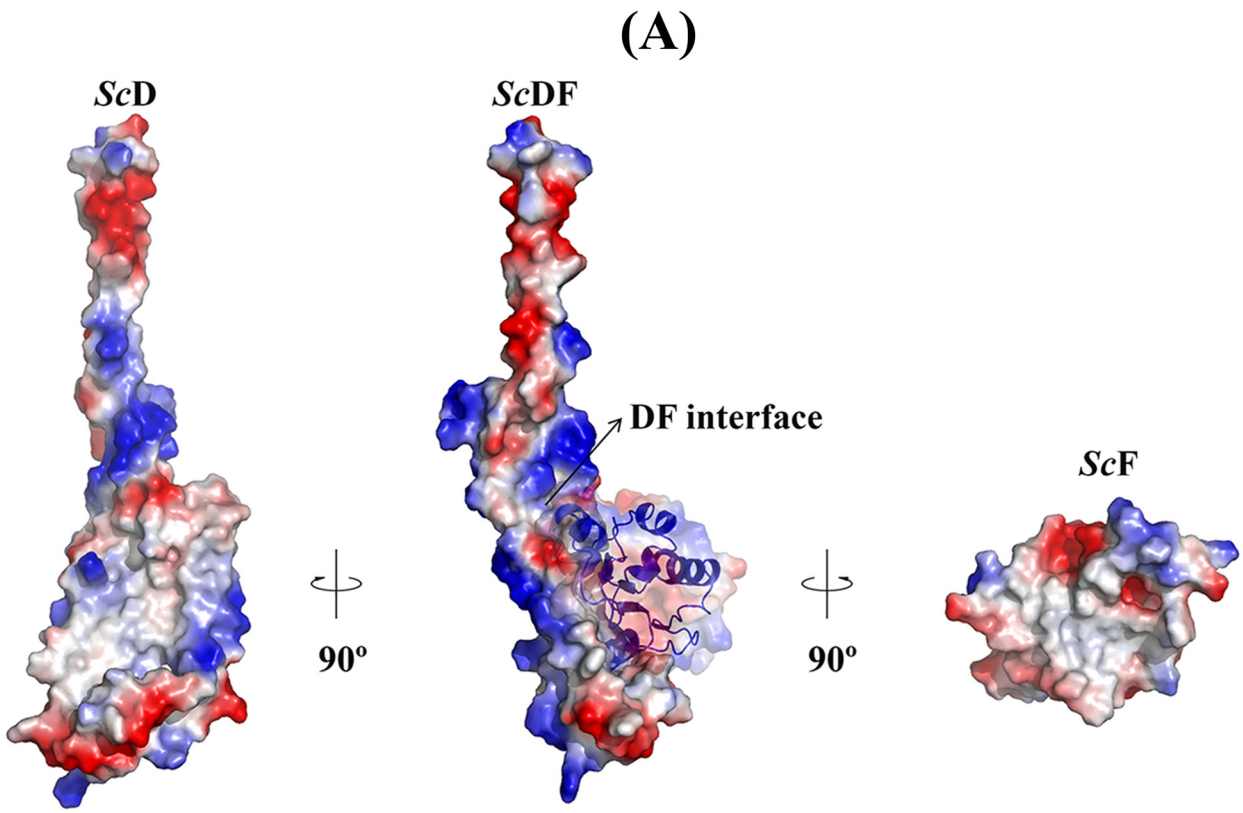

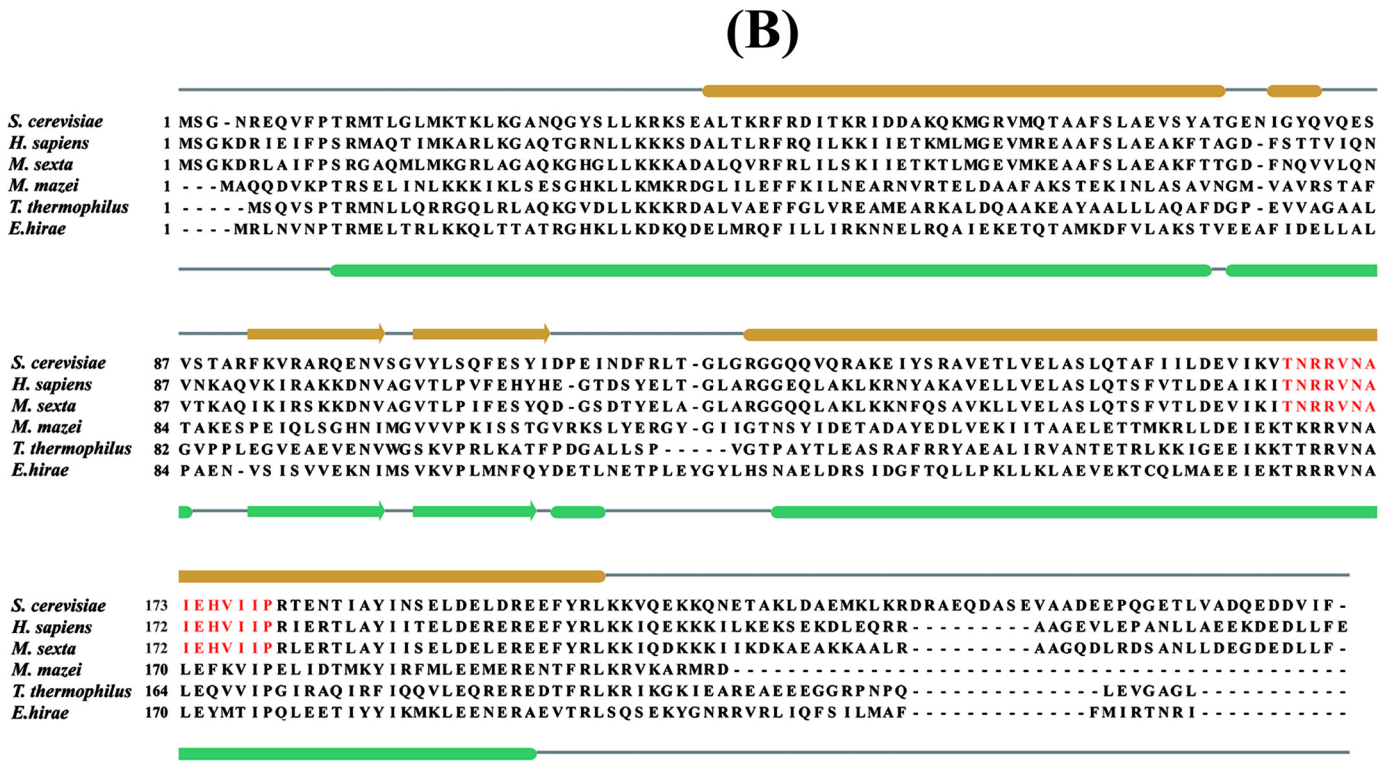

FIGURE 3. **Surface electrostatic and hydrophobicity of DF assembly and sequence comparison of subunit D.** *A,* surface electrostatic potential of the *Sc*DF complex with *Sc*F shown as schematic and the DF interface labeled by an *arrow* is shown in the center. Surface electrostatic potential of *Sc*D reveals that the interacting surface with *Sc*F is mostly hydrophobic, whereas the exposed N and C termini of *Sc*D are composed of basic and predominantly acidic residues (*left*). The interacting surface of *Sc*F is predominantly hydrophobic (*right*). The electrostatic potential surfaces were calculated using APBS (56) and mapped at contouring levels from −3 *kT* (*blue*) to 3 *kT* (*red*). *B,* sequence alignment of subunit D from different V-ATPases and ATP synthases, respectively. The secondary structure elements of subunit D of the *E. hirae* A-ATP synthase and the *S. cerevisiae* V-ATPase are shown. The conserved sequence in the eukaryotic V-ATPases is highlighted in *red*.

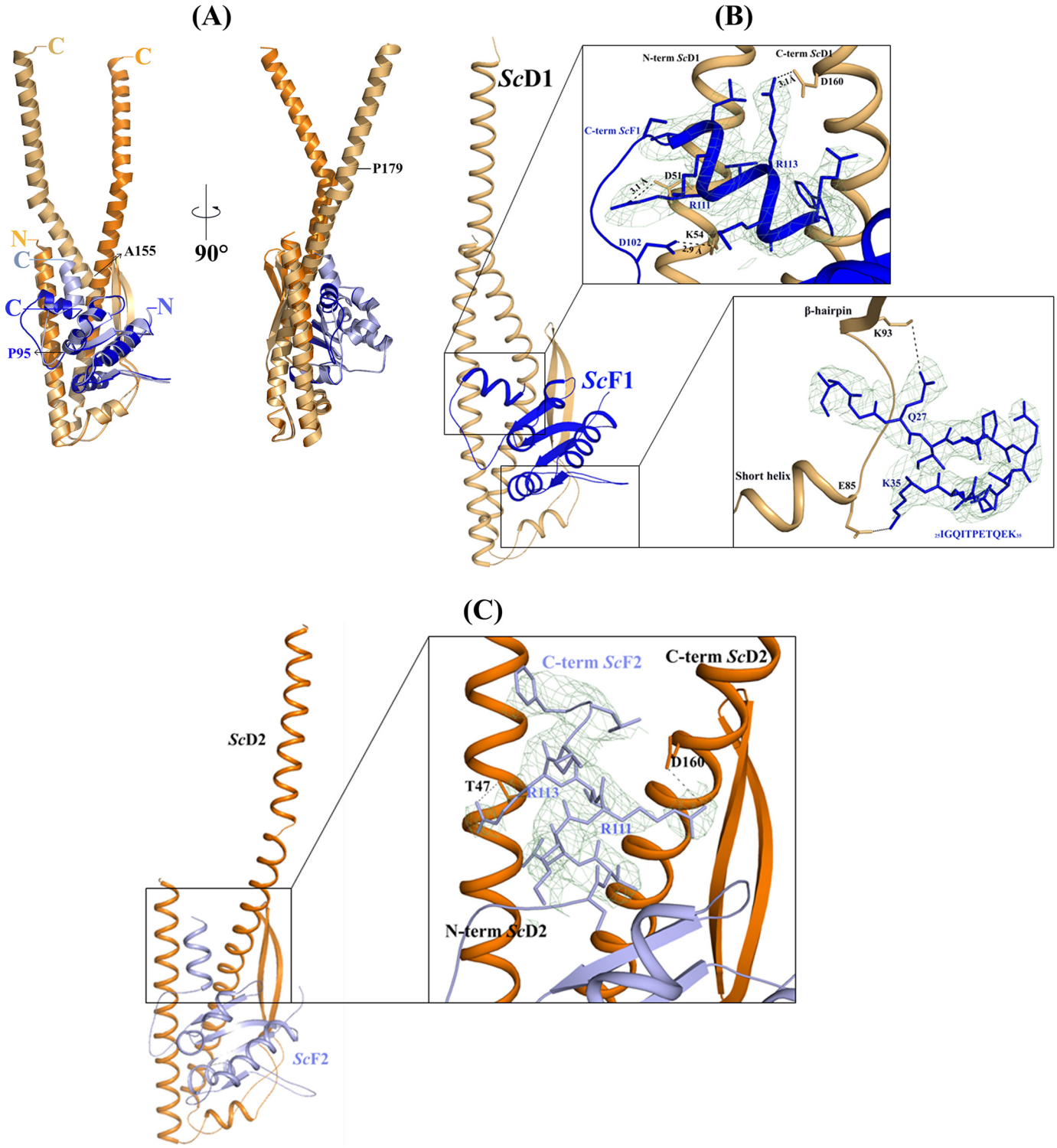

FIGURE 4. **Intermolecular interactions of DF assembly.** *A,* superimposition of the *Sc*DF1 (*wheat* and *blue*) with *Sc*DF2 molecule (*orange* and *light blue*). Residues Ala-155 and Pro-179 of subunit D and Pro-95 of subunit F are labeled. *B,* interactions in the *Sc*DF1 molecule. The interaction of the very C terminus of *Sc*F1 compact form with the N and C terminus of *Sc*D1, and the interaction of the loop ^{25}IGQITPETQEK^{35} of *Sc*F1 with the loop between the short helix and β hairpin region of *Sc*D1 are shown in the *inset*, respectively. *C, Sc*DF2 molecule, where the *Sc*F2 C-terminal helix is almost parallel to the N- and C-terminal helix of *Sc*D2, is shown as schematic. *Inset,* interactions of the C-terminal helix of *Sc*F2 is presented. The electron density omit map (contoured at 2σ) is shown in *green mesh*.

and *D*). These data reveal that the C-terminal region of subunit F can undergo dynamic movements in solution.

DISCUSSION

The crystallographic structure of subunit F of the *Sc*DF1 and *Sc*DF2 molecule of the *S. cerevisiae* V-ATPase, respectively, and the recently determined structure of the N-terminal domain of subunit F, *Sc*F(1–94) ((18) including the N-terminal residues 1–94) show an r.m.s.d. value 1.42 and 1.5 Å, respectively, indicating no major difference in the globular domain of these structures. The present entire structure (118 amino acids) of

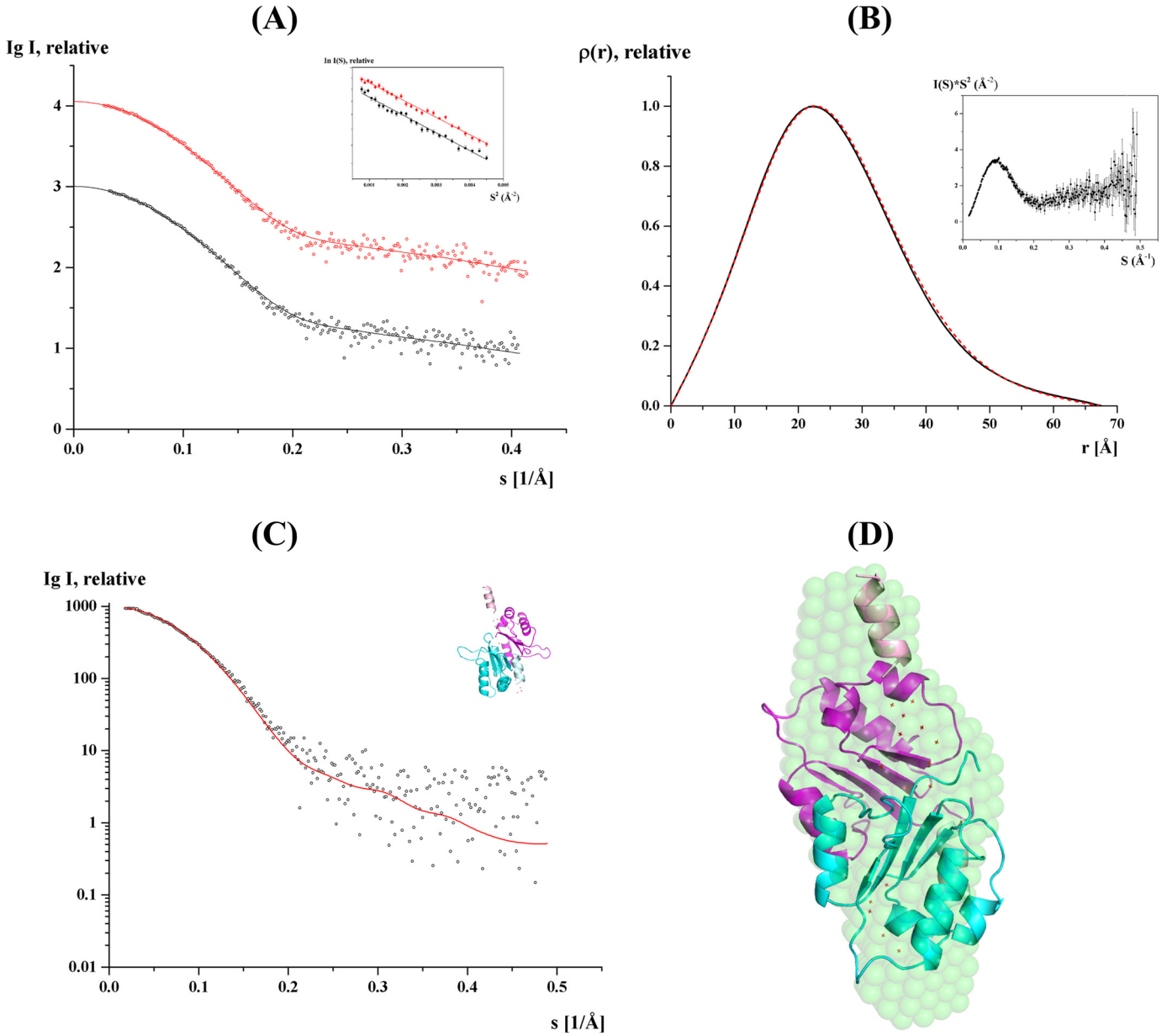

FIGURE 5. **Solution x-ray scattering studies of *Sc*F.** *A*, small angle x-ray scattering pattern (○) and its corresponding experimental fitting curves (- - -) for the concentrations 2.0 (*black*) and 4.2 (*red*) mg/ml. The scattering curves of *Sc*F are displayed in logarithmic units for clarity. *Inset*, Guinier plots show linearity for the concentrations used, indicating no aggregation. *B*, pair-distance distribution function *P*(*r*) of *Sc*F at 2.0 (*black*) and 4.2 (*red*) mg/ml. *Inset*, Kratky plot of *Sc*F SAXS data at 4.2 mg/ml. *C*, fit of the scattering profile of the CORAL model with the best χ value of 1.24 (*red*) to the experimental scattering pattern of *Sc*F at 2 mg/ml (*black*). *D*, CORAL model generated is superimposed with the solution shape of *Sc*F. The compact monomer of the dimer is colored *cyan*, and the extended monomer is colored *magenta*. The C-terminal helices are colored lighter and the flexible regions are represented as *dots* and colored *red*.

*Sc*F in the *Sc*DF1 molecule as well as the 116-amino acid structure of subunit F in the *Sc*DF2 molecule give insights of the important C terminus with its flexible loop (Pro-95–Asp-106) and helix α5. The comparison of both subunit F structures (Fig. 4*A*) reveals differences mainly in the C terminus of both molecules indicated by the high r.m.s.d. value (3.58 Å). The Pro-95–Asp-106-loop with its bent feature at Lys-105 enables structural rearrangements, leading to a perpendicular or parallel orientation of helix α5 relative to the N- and C-terminal helix of subunit D (Fig. 4*A*). The solution x-ray scattering data of *S. cerevisiae* V-ATPase subunit F confirm the flexibility of the Pro-95–Asp-106 loop and demonstrate that this loop and helix α5 are able to undergo a rearrangement from a compact subunit F to an extended C-terminal formation (Fig. 5*D*). These data extend the recent findings of ^{15}N-(^{1}H) heteronuclear NOE studies on *Sc*F, demonstrating that helix α5 with the adjacent Pro-95–Asp-106 loop is flexible in solution (18). As demonstrated by the structure of the *Sc*DF1 and *Sc*DF2 molecules, the flexibility of the C-terminal segment of *Sc*F leads to different interactions with the rotary subunit D, in which the C terminus of subunit F is either in proximity to the subunit D residues Asp-51, Lys-54, and Asp-160 (*Sc*DF1 molecule) or with the subunit D amino acids as Thr-47 and Asp-160 (*Sc*DF2 molecule; Fig. 4*C*). We showed most recently that subunit F of the eukaryotic *S. cerevisiae* V-ATPase activates ATP hydrolysis of the related archaea A_1 complex, in which *Sc*F was reconstituted

TABLE 2
Data collection and scattering derived parameters for *Sc*F using SAXS

Data collection parameters	
Instrument	Bruker NANOSTAR
Beam geometry	100-μm slit
Wavelength (Å)	1.3414
q range (Å^{-1})	0.01–0.5
Exposure time (min)	30
Concentration range (mg/ml)	2 and 4.2
Temperature (K)	288
Structural parameters[a]	
$I(0)$ (cm^{-1}) (from $P(r)$)	999.9 ± 7
R_g (Å) (from $P(r)$)	19.6 ± 0.3
$I(0)$ (cm^{-1}) (from Guinier)	1007 ± 7
R_g (Å) (from Guinier)	19.3 ± 0.6
D_{max} (Å)	67.5 ± 3
Porod volume estimate (Å^3)	~32,831
Dry volume calculated from sequence (Å^3)	15,903
Molecular mass determination[a]	
Calculated monomeric M_r from sequence	13,144
M_r from $I(0)$	21,305
M_r from SAXS MoW	24,100
M_r from excluded volume	23,200
Software employed	
Primary data reduction	SAXS
Data processing	PRIMUS
Ab initio analysis	DAMMIN
Validation and averaging	DAMAVER
Rigid body modeling	CORAL
Computation of model intensities	CRYSOL
Three-dimensional graphics representations	PyMOL

[a] Data are reported for 2 mg/ml measurements.

with the A_3B_3D complex of the archaeal *Methanococcus mazei* Gö1 A-ATP synthase.[5] In the same set of experiments, it was demonstrated that no A_3B_3DF complex could be formed when the C-terminal truncated *Sc*F(1–94) was used, which underlines the need of the C terminus of subunit F for proper assembly and enzyme activity.

The question arises to how the Pro-95–Asp-106-loop with helix α5 of *Sc*F connects the activation of ATP hydrolysis in the catalytic A_3B_3 headpiece of the enzyme. When the presented *Sc*DF1 and *Sc*DF2 molecules, respectively, were docked into the nucleotide-bound A_3B_3 headpiece of the related *E. hirae* A-ATP synthase (26), no interaction between the compact form of *Sc*F (*Sc*DF1 molecule) and the nucleotide-binding subunits A or B was observed. In comparison, Lys-114 of the extended α5 helix of subunit F (*Sc*DF2 molecule) comes in close proximity (3.3 Å) to Asp-480 of the AMP-PNP-bound catalytic A subunit (Fig. 6*A*), allowing a direct coupling between the catalytic A subunit and the central stalk subunit F. The subunit A–F arrangement confirms the requirement for the very C terminus of subunit F, as described by the C-terminal truncated *Sc*F(1–94) above.[5]

As shown for the related bacterial F-ATP synthase, the central stalk subunits γε in $\alpha_3\beta_3\gamma\epsilon$ complexes, which are proposed to be homologues to the DF assembly, and the A_3B_3 headpiece of V-ATPases, rotate in 80° and 40° substeps (57–60), or as most recently shown for the human mitochondrial F_1-ATPase subunit, γ rotates in three 120° steps with sub-steps of 0–65, 65–90, and 90–120° (61). Here, we moved the DF assembly inside the A_3B_3 shaft by 80° and observed that amino acid Lys-114 of the extended helix α5 of *Sc*F comes in the neighborhood to Glu-391 of subunit B, belonging to the C-terminal region ^{388}VLGESALSDI^{397} of subunit B (Fig. 6, *B* and *C*), which occupies a similar position to the so-called DELSEED region of the nucleotide-binding subunits α and β of F_1F_0-ATP synthases (62). At the same time the subunit F residues Arg-80, Arg-83, and Thr-51, Asp-52, Asn-55, Glu-59, Glu-60 of helix 2 and helix 4, respectively, are close to subunit A residues Ile-584, Val-585, Ser-586, and Asn-543, Glu-544, Glu-547, Gly-548, respectively (Fig. 6*B*). These interactions of subunit F with several subunit A and B residues may change the nucleotide-binding and ATP cleavage steps in the catalytic subunit A. The 80° movement of the DF assembly also brings the bended C-terminal helix of *Sc*D in the interface of the nucleotide-free subunits A and B (Fig. 6*D*), where the amino acids Asn-190 and Glu-199 come in proximity to the residue Thr-439 and Lys-335 of subunit A and B, respectively. In the future, single molecule rotation studies of the *S. cerevisiae* A_3B_3DF complex may provide more details about sub-steps of the central stalk subunits DF inside the V_1-ATPase. This will be of great interest, because subunit F and ε reveal no structural similarity, and subunits D and γ are similar in respect to their N- and C-terminal helices. When the globular domain of the *E. coli* subunit γ (*Ec*γ) was superimposed with *Sc*F, a similar fold of both domains could be observed with respect to the central parallel β-sheet (β1–β3), which is flanked by the α-helices α1 and α2 on both sides of its plane (Fig. 7). The sequence similarity of the globular domain of *Ec*γ and *Sc*F is 18.9%. Future studies may show whether subunit γ is a fused form of subunits D and F of eukaryotic V-ATPases as well as the related and evolutionary older A-ATP synthases, respectively (5).

The structural differences observed in the C terminus of subunit F in the *Sc*DF1 and *Sc*DF2 molecules of our presented structure depicts not only two mechanistically relevant conformations but also shows the stabilizing effect in the DF complex via the formation of salt bridges at the interface of the C termini of both subunits. The perpendicular orientation of *Sc*F helix α5 relative to the N- and C-terminal helix of subunit D leads to the interaction of Asp-51 and Asp-160 of *Sc*D (*Sc*DF1 molecule) with amino acids Arg-111 and Arg-113 of subunit D, respectively (Fig. 4*B*). This may stabilize the coiled coil formation during rotary steps of the central DF assemblage. As shown for the *E. hirae* A-ATP synthase, depletion of the C-terminal residues of subunit F led to insolubility of subunit D, indicating the stabilizing role of the C terminus of subunit F in DF formation (26).

As described recently and confirmed here, subunit F of eukaryotic V-ATPases contains the conserved ^{26}GQITPETQEK^{35} loop (Fig. 4*B*), which faces the C-terminal serine residue Ser-381 of subunit H (18), revealed to be involved in F-H cross-linking formation (Fig. 1) (18, 63). It has been proposed that in the process of V_1 and V_O dissociation, the flexible C-terminal domain of subunit H moves slightly closer to its nearest neighbor, the exposed ^{26}GQITPETQEK^{35} loop of subunit F, where it causes conformational changes, leading to an inhibitory effect of ATPase activity in the V_1-ATPase (18, 63). The present *Sc*DF structure shows for the first time that the unique ^{26}GQITPETQEK^{35} loop of *Sc*F is within 4 Å of the ^{85}ESVSTARFK^{93} loop of *Sc*D. The two hydrogen bonding inter-

[5] D. Singh, H. Sielaff, A. Grüber, G. Biuković, L. Sundararaman, S. Bhushan, T. Wohland, and G. Grüber, submitted for publication.

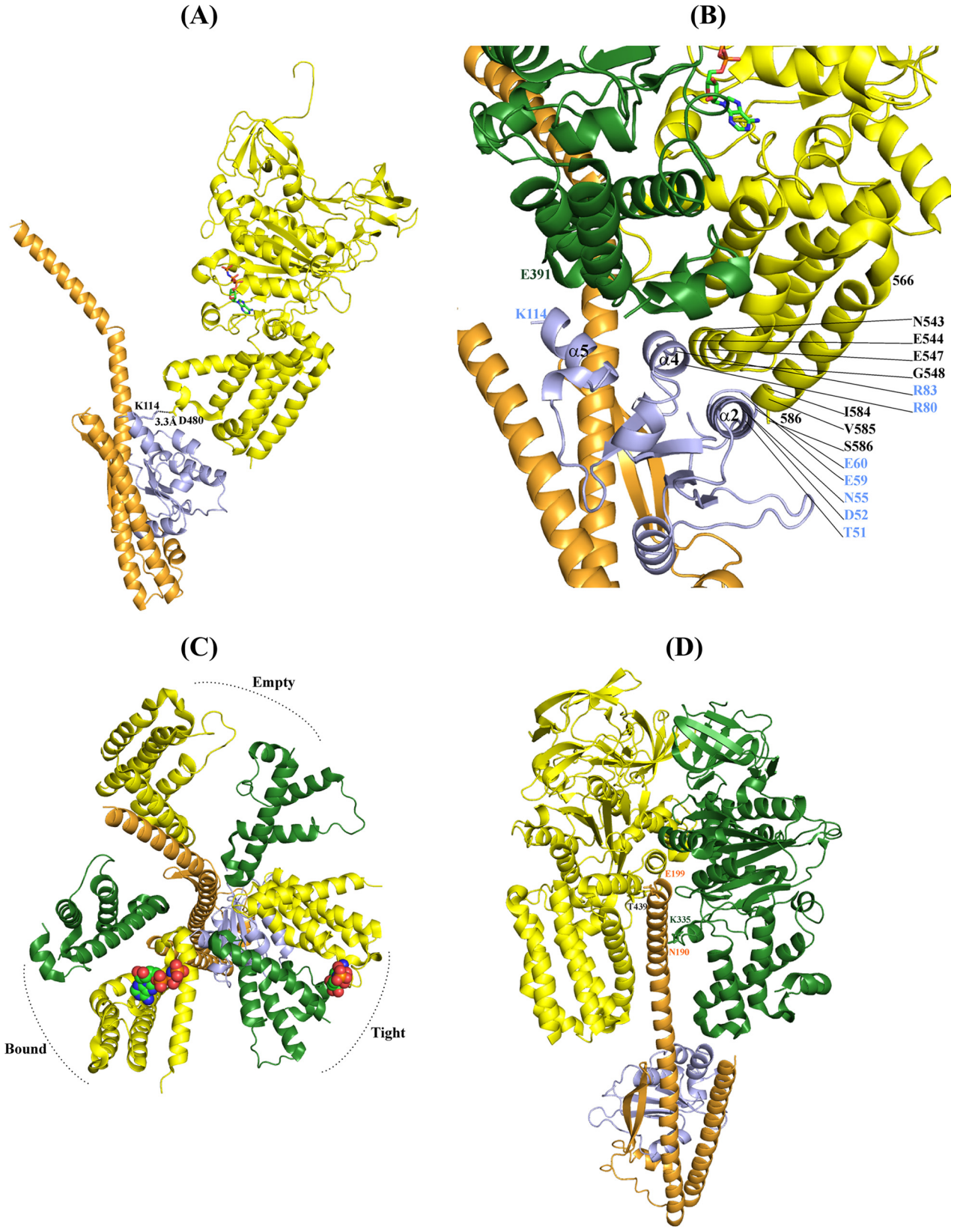

FIGURE 6. **Fitting of the *Sc*DF onto the DF subunits of the nucleotide-bound *E. hirae* A_1-ATP synthase structure (3VR6 (26)).** *A,* extended C terminus of *Sc*F (*Sc*DF2 molecule) comes in contact with the *Eh*A with the residue Lys-114 of *Sc*F2 having electrostatic interaction with Asp-480 of *Eh*A. Only one subunit A from *E. hirae* hexamer is shown for clarity. The nucleotide is shown in *stick* representation. *B,* close view of the various interactions of the extended *Sc*F with *Eh*A and B in the tight form of the A-B interface when *Sc*DF2 is rotated by 80°. The α2 and α4 of *Sc*F interacts with the C-terminal domain of *Eh*A and α5 interacts with *Eh*B. *C,* top view showing the C-terminal domain of subunit A and B from *E. hirae* A_1-ATP synthase and the position of *Sc*DF2 after 80° rotation. *Sc*F is in close proximity to the tight form of the nucleotide-binding site, and *Sc*D lies between the empty and bound forms. *D,* interaction of *Sc*D with subunits A and B of *E. hirae*. For clarity other subunits are removed from the hexamer.

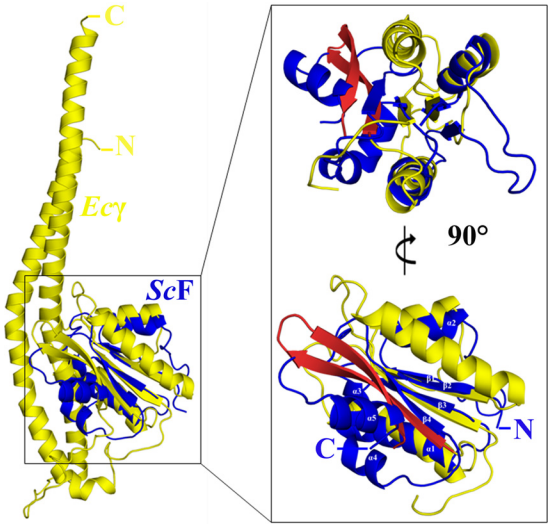

FIGURE 7. **Superposition of subunit γ of the *E. coli* F-ATP synthase with *Sc*F.** Overall superposition of the *E. coli* subunit γ ((51) 3OAA; *yellow*) with *Sc*F subunit (4RND; *blue*). *Inset,* globular domain of the γ subunit shares a similar fold with *Sc*F. The α-helices and β-strands of *Sc*F are labeled. The β-hairpin of *Ec*γ is shown in *red*. Two views of the superposition, rotated by 90°, are shown for clarity.

actions between the guanidine side chain of subunit D residue Lys-93 and the carbonyl side chain of *Sc*F residue Gln-27 as well as the one between Gln-84 of *Sc*D and Lys-35 of *Sc*F may play significant roles in this interaction. Interestingly, amino acid Lys-93 is highly conserved in subunit D of eukaryotic V-ATPases and is located at the beginning of the β-hairpin (Fig. 4*B*), which is reported to stimulate ATPase activity 2-fold in the bacterial *E. hirae* A-ATP synthase (25). Furthermore, amino acid Glu-85 is located at the end of the short helix (^{79}IGYQVQE^{85}) of subunit D. This short helix is discussed to be involved in energy coupling and to play an important role in reversible disassembly (18).

^{15}N^{1}H heteronuclear NOE studies on the *S. cerevisiae* subunit F revealed a rigid core formed by β-strands, β1 to β4, and α2 to α4. In comparison, the N- and C-terminal helices α1 and α5 with their adjacent loops ^{26}GQITPETQEK^{35} and ^{94}IPSKDHPYD^{102}, respectively, are more flexible in solution (18). The N-terminal helix α1 of subunit F and the bottom segment of subunit D form the neighborhood with subunit *d* (18). It has been proposed that this area is important during the process of dissociation and reassembly of the V_1 and V_O sectors. In this scenario, the higher flexibility of α1 in subunit F would allow transmission of a change in subunit *d* during dissociation from the DF heterodimer and also the movement of subunit H closer to F, via the neighboring ^{26}GQITPETQEK^{35} loop (18). In the latter case, the signal of V_1V_O disassembly may be communicated by the ^{26}GQITPETQEK^{35} loop to the neighboring ^{85}ESVSTARFK^{93} loop of *Sc*D and in turn to the short helix (^{79}IGYQVQE^{85}) as well as the β-hairpin of subunit D. In addition, the ^{26}GQITPETQEK^{35} loop would transfer the H to F movement via the second flexible ^{94}IPSKDHPYD^{102} loop, which is adjacent to helix α5. Subsequently, helix α5 moves from its extended position away from the catalytic A subunit to the perpendicular orientation, leading to reduction of ATPase activity.

Acknowledgments—We thank the National Synchrotron Radiation Research Center, a national user facility supported by the National Science Council of Taiwan. We thank the staff at the Synchrotron Radiation Protein Crystallography Facility (supported by the National Research Program for Genomic Medicine) at beam line 13B1 for expert help with data collection. We sincerely thank Dr. Kamariah Neelagandan for data collection at the 13B1 National Synchrotron Radiation Research Center, Taiwan. We are grateful to Prof. R. Kraut and Dr. G. Tria from the School of Biological Sciences, Nanyang Technological University, for reading the manuscript.

REFERENCES

1. Kluge, C., Lahr, J., Hanitzsch, M., Bolte, S., Golldack, D., and Dietz, K. J. (2003) New insight into the structure and regulation of the plant vacuolar H^+-ATPase. *J. Bioenerg. Biomembr.* **35,** 377–388
2. Saroussi, S., and Nelson, N. (2009) Vacuolar H^+-ATPase–an enzyme for all seasons. *Pflügers Arch.* **457,** 581–587
3. Beyenbach, K. W., and Wieczorek, H. (2006) The V-type H^+ ATPase: molecular structure and function, physiological roles and regulation. *J. Exp. Biol.* **209,** 577–589
4. Nishi, T., and Forgac, M. (2002) The vacuolar (H^+)-ATPases–nature's most versatile proton pumps. *Nat. Rev. Mol. Cell Biol.* **3,** 94–103
5. Marshansky, V., Rubinstein, J. L., and Grüber, G. (2014) Eukaryotic V-ATPase: novel structural findings and functional insights. *Biochim. Biophys. Acta* **1837,** 857–879
6. Wilkens, S. (2001) Structure of the vacuolar adenosine triphosphatases. *Cell Biochem. Biophys.* **34,** 191–208
7. Graham, L. A., Flannery, A. R., and Stevens, T. H. (2003) Structure and assembly of the yeast V-ATPase. *J. Bioenerg. Biomembr.* **35,** 301–312
8. Radermacher, M., Ruiz, T., Wieczorek, H., and Grüber, G. (2001) The structure of the V_1-ATPase determined by three-dimensional electron microscopy of single particles. *J. Struct. Biol.* **135,** 26–37
9. Lolkema, J. S., Chaban, Y., and Boekema, E. J. (2003) Subunit composition, structure, and distribution of bacterial V-type ATPases. *J. Bioenerg. Biomembr.* **35,** 323–335
10. Muench, S. P., Scheres, S. H., Huss, M., Phillips, C., Vitavska, O., Wieczorek, H., Trinick, J., and Harrison, M. A. (2014) Subunit positioning and stator filament stiffness in regulation and power transmission in the V_1 motor of the *Manduca sexta* V-ATPase. *J. Mol. Biol.* **426,** 286–300
11. Benlekbir, S., Bueler, S. A., and Rubinstein, J. L. (2012) Structure of the vacuolar-type ATPase from *Saccharomyces cerevisiae* at 11-A resolution. *Nat. Struct. Mol. Biol.* **19,** 1356–1362
12. Svergun, D. I., Konrad, S., Huss, M., Koch, M. H., Wieczorek, H., Altendorf, K., Volkov, V. V., and Grüber, G. (1998) Quaternary structure of V_1 and F_1 ATPase: significance of structural homologies and diversities. *Biochemistry* **37,** 17659–17663
13. Diepholz, M., Venzke, D., Prinz, S., Batisse, C., Flörchinger, B., Rössle, M., Svergun, D. I., Böttcher, B., and Féthière, J. (2008) A different conformation for EGC stator subcomplex in solution and in the assembled yeast V-ATPase: possible implications for regulatory disassembly. *Structure* **16,** 1789–1798
14. Drory, O., Frolow, F., and Nelson, N. (2004) Crystal structure of yeast V-ATPase subunit C reveals its stator function. *EMBO Rep.* **5,** 1148–1152
15. Oot, R. A., Huang, L.-S., Berry, E. A., and Wilkens, S. (2012) Crystal structure of the yeast vacuolar ATPase heterotrimeric EGC-head peripheral stalk complex. *Structure* **20,** 1881–1892
16. Rishikesan, S., Thaker, Y. R., and Grüber, G. (2011) NMR solution structure of subunit E (fragment E(1–69)) of the *Saccharomyces cerevisiae* V_1V_O ATPase. *J. Bioenerg. Biomembr.* **43,** 187–193
17. Rishikesan, S., and Grüber, G. (2011) Structural elements of the C-terminal domain of subunit E ($E_{133–222}$) from the *Saccharomyces cerevisiae* V_1V_O ATPase determined by solution NMR spectroscopy. *J. Bioenerg. Biomembr.* **43,** 447–455
18. Basak, S., Lim, J., Manimekalai, M. S., Balakrishna, A. M., Grüber, G. (2013) Crystal and NMR structures give insights into the role and dynam-

ics of subunit F of the eukaryotic V-ATPase from *Saccharomyces cerevisiae*. *J. Biol. Chem.* **288,** 11930–11939
19. Rishikesan, S., Gayen, S., Thaker, Y. R., Vivekanandan, S., Manimekalai, M. S., Yau, Y. H., Shochat, S. G., and Grüber, G. (2009) Assembly of subunit *d* (Vma6p) and G (Vma10p) and the NMR solution structure of subunit G (G_{1-59}) of the *Saccharomyces cerevisiae* V_1V_O ATPase. *Biochim. Biophys. Acta* **1787,** 242–251
20. Rishikesan, S., Manimekalai, M. S., and Grüber, G. (2010) The NMR solution structure of subunit G (G_{61-101}) of the eukaryotic V_1V_O ATPase from *Saccharomyces cerevisiae*. *Biochim. Biophys. Acta* **1798,** 1961–1968
21. Sagermann, M., Stevens, T. H., and Matthews, B. W. (2001) Crystal structure of the regulatory subunit H of the V-type ATPase of *Saccharomyces cerevisiae*. *Proc. Natl. Acad. Sci. U.S.A.* **98,** 7134–7139
22. Grüber, G., Radermacher, M., Ruiz, T., Godovac-Zimmermann, J., Canas, B., Kleine-Kohlbrecher, D., Huss, M., Harvey, W. R., and Wieczorek, H. (2000) Three-dimensional structure and subunit topology of the V_1 ATPase from *Manduca sexta* midgut. *Biochemistry* **39,** 8609–8616
23. Coskun, U., Rizzo, V. F., Koch, M. H., and Grüber, G. (2004) Ligand-dependent structural changes in the V_1 ATPase from *Manduca sexta*. *J. Bioenerg. Biomembr.* **36,** 249–256
24. Futai, M., Nakanishi-Matsui, M., Okamoto, H., Sekiya, M., and Nakamoto, R. K. (2012) Rotational catalysis in proton pumping ATPases: from *E. coli* F-ATPase to mammalian V-ATPase. *Biochim. Biophys. Acta* **1817,** 1711–1721
25. Saijo, S., Arai, S., Hossain, K. M., Yamato, I., Suzuki, K., Kakinuma, Y., Ishizuka-Katsura, Y., Ohsawa, N., Terada, T., Shirouzu, M., Yokoyama, S., Iwata, S., and Murata, T. (2011) Crystal structure of the central axis DF complex of the prokaryotic V-ATPase. *Proc. Natl. Acad. Sci. U.S.A.* **108,** 19955–19960
26. Arai, S., Saijo, S., Suzuki, K., Mizutani, K., Kakinuma, Y., Ishizuka-Katsura, Y., Ohsawa, N., Terada T., Shirouzu, M., Yokoyama, S., Iwata, S., Yamato, I., and Murata, T. (2013) Rotation mechanism of *Enterococcus hirae* V_1-ATPase based on asymmetric crystal structures. *Nature* **493,** 703–707
27. Nagamatsu, Y., Takeda, K., Kuranaga, T., Numoto, N., and Miki, K. (2013) Origin of asymmetry at the intersubunit interfaces of V_1-ATPase from *Thermus thermophilus*. *J. Mol. Biol.* **425,** 2699–2708
28. Otwinowski, Z., and Minor, W. (1997) Processing of X-ray diffraction data collected in oscillation mode. *Methods Enzymol.* **276,** 307–326
29. Karplus, P. A., and Diederichs, K. (2012) Linking crystallographic model and data quality. *Science* **336,** 1030–1033
30. Adams, P. D., Afonine, P. V., Bunkóczi, G., Chen, V. B., Davis, I. W., Echols, N., Headd, J. J., Hung, L. W., Kapral, G. J., Grosse-Kunstleve, R. W., McCoy, A. J., Moriarty N. W., Oeffner, R., Read, R. J., Richardson, D. C., Richardson, J. S., Terwilliger, T. C., and Zwart, P. H. (2010) PHENIX: a comprehensive Python-based system for macromolecular structure solution. *Acta Crystallogr. D Biol. Crystallogr.* **66,** 213–221
31. Sheldrick, G. M. (2010) Experimental phasing with SHELXC/D/E: combining chain tracing with density modification. *Acta Crystallogr. D Biol. Crystallogr.* **66,** 479–485
32. Panjikar, S., Parthasarathy, V., Lamzin, V. S., Weiss, M. S., and Tucker, P. A. (2005) Auto-Rickshaw: an automated crystal structure determination platform as an efficient tool for the validation of an X-ray diffraction experiment. *Acta Crystallogr. D Biol. Crystallogr.* **61,** 449–457
33. Panjikar S., Parthasarathy, V., Lamzin, V. S., Weiss, M. S., and Tucker, P. A. (2009) On the combination of molecular replacement and single anomalous diffraction phasing for automated structure determination. *Acta Crystallogr. D Biol. Crystallogr.* **65,** 1089–1097
34. Cowtan, K. (2000) General quadratic functions in real and reciprocal space and their application to likelihood phasing. *Acta Crystallogr. D Biol. Crystallogr.* **56,** 1612–1621
35. Cowtan, K. (2006) The Buccaneer software for automated model building. 1. Tracing protein chains. *Acta Crystallogr. D Biol. Crystallogr.* **62,** 1002–1011
36. Emsley, P., and Cowtan, K. (2004) COOT: model-building tools for molecular graphics. *Acta Crystallogr. D Biol. Crystallogr.* **60,** 2126–2132
37. Murshudov, G. N., Vagin, A. A., and Dodson, E. J. (1997) Refinement of macromolecular structures by the maximum-likelihood method. *Acta Crystallogr. D Biol. Crystallogr.* **53,** 240–255
38. Laskowski, R. A., MacArthur, M. W., Moss, D. S., and Thornton, J. M. (1993) PROCHECK: a program to check the stereochemical quality of protein structures. *J. Appl. Cryst.* **26,** 283–291
39. Chen, V. B., Arendall, W. B., 3rd, Headd, J. J., Keedy, D. A., Immormino, R. M., Kapral, G. J., Murray, L. W., Richardson, J. S., and Richardson, D. C. (2010) MolProbity: all-atom structure validation for macromolecular crystallography. *Acta Crystallogr. D Biol. Crystallogr.* **66,** 12–21
40. DeLano, W. (2002) *The PyMOL Molecular Graphics System,* version 1.5.0.4. DeLano Scientific, San Carlos, CA
41. Dip, P. V., Kamariah, N., Subramanian Manimekalai, M. S., Nartey, W., Balakrishna, A. M., Eisenhaber, F., Eisenhaber, B., and Grüber, G. (2014) Structure, mechanism and ensemble formation of the alkylhydroperoxide reductase subunits AhpC and AhpF from *Escherichia coli*. *Acta Crystallogr. D Biol. Crystallogr.* **70,** 2848–2862
42. Konarev, P. V., Volkov, V. V., Sokolova, A. V., Koch, M. H., and Svergun, D. I. (2003) PRIMUS- a Windows-PC based system for small-angle scattering data analysis. *J. Appl. Cryst.* **36,** 1277–1282
43. Guinier, A., and Fournet, G. (1955) *Small-angle Scattering of X-rays* (translated from French by C. B. Walker) pp. 5–78. John Wiley & Sons, Inc., New York
44. Glatter, O., and Kratky, O. (eds) (1982) *Small-angle X-ray Scattering.* pp. 17–51, Academic Press, London, UK
45. Svergun, D. (1992) Determination of the regularization parameter in indirect-transform methods using perceptual criteria. *J. Appl. Cryst.* **25,** 495–503
46. Mertens, H. D., and Svergun, D. I. (2010) Structural characterization of proteins and complexes using small-angle x-ray solution scattering. *J. Struct. Biol.* **172,** 128–141
47. Svergun, D. I. (1999) Restoring low resolution structure of biological macromolecules from solution scattering using simulated annealing. *Biophys. J.* **76,** 2879–2886
48. Kozin, M. B., and Svergun, D. I. (2001) Automated matching of high- and low-resolution structural models. *J. Appl. Cryst.* **34,** 33–41
49. Volkov, V. V., and Svergun, D. I. (2003) Uniqueness of *ab initio* shape determination in small-angle scattering. *J. Appl. Cryst.* **36,** 860–864
50. Svergun D. I., Barberato C., and Koch M. H. J. (1995) CRYSOL–a program to evaluate x-ray solution scattering of biological macromolecules from atomic coordinates. *J. Appl. Cryst.* **28,** 768–773
51. Shah, N. B., Hutcheon, M. L., Haarer, B. K., and Duncan, T. M. (2013) The ϵ inhibited state forms after ATP hydrolysis, is distinct from the ADP-inhibited state, and responds dynamically to catalytic site ligands. *J. Biol. Chem.* **288,** 9383–9395
52. Petoukhov, M. V., Franke, D., Shkumatov, A. V., Tria, G., Kikhney, A. G., Gajda, M., Gorba, C., Mertens, H. D., Konarev, P. V., and Svergun, D. I. (2012) New developments in the ATSAS program package for small-angle scattering data analysis. *J. Appl. Cryst.* **45,** 342–350
53. Matthews, B. W. (1968) Solvent content of protein crystals. *J. Mol. Biol.* **33,** 491–497
54. Colovos, C., and Yeates, T. O. (1993) Verification of protein structures: patterns of nonbonded atomic interactions. *Protein Sci.* **2,** 1511–1519
55. Fischer, H., de Oliveira Neto, M., Napolitano, H. B., Polikarpov, I., and Craievich, A. F. (2010) Determination of the molecular weight of proteins in solution from a single small-angle x-ray scattering measurement on a relative scale. *J. Appl. Cryst.* **43,** 101–109
56. Baker, N. A., Sept, D., Joseph, S., Holst, M. J., and McCammon, J. A. (2001) Electrostatics of nanosystems: application to microtubules and the ribosome. *Proc. Natl. Acad. Sci. U.S.A.* **98,** 10037–10041
57. Yasuda, R., Noji, H., Yoshida, M., Kinosita, K., Jr., and Itoh, H. (2001) Resolution of distinct rotational substeps by submillisecond kinetic analysis of F_1-ATPase. *Nature* **410,** 898–904
58. Martin, J. L., Ishmukhametov, R., Hornung, T., Ahmad, Z., and Frasch, W. D. (2014) Anatomy of F_1-ATPase powered rotation. *Proc. Natl. Acad. Sci. U.S.A.* **111,** 3715–3720
59. Sielaff, H., Rennekamp, H., Engelbrecht, S., and Junge, W. (2008) Functional halt positions of rotary F_OF_1-ATPase correlated with crystal structures. *Biophys. J.* **95,** 4979–4987
60. Nakanishi-Matsui, M., Kashiwagi, S., Hosokawa, H., Cipriano, D. J., Dunn,

S. D., Wada, Y., and Futai, M. (2006) Stochastic high-speed rotation of *Escherichia coli* ATP synthase F_1 sector: the ϵ subunit-sensitive rotation. *J. Biol. Chem.* **281,** 4126–4131

61. Suzuki, T., Tanaka, K., Wakabayashi, C., Saita, E.-I., and Yoshida, M. (2014) Chemomechanical coupling of human mitochondrial F1-ATPase motor. *Nat. Chem. Biol.* **10,** 930–936
62. Aggeler, R., and Capaldi, R. A. (1996) Nucleotide-dependent movement of the ϵ subunit between α and β subunits in the *Escherichia coli* F_1F_0-type ATPase. *J. Biol. Chem.* **271,** 13888–13891
63. Jefferies, K. C., and Forgac, M. (2008) Subunit H of the vacuolar (H^+) ATPase inhibits ATP hydrolysis by the free V_1 domain by interaction with the rotary subunit F. *J. Biol. Chem.* **283,** 4512–4519